ACSNANO

www.acsnano.org

ARTICLE

Rationally Designed Topological Quantum Dots in Bottom-Up Graphene Nanoribbons

Daniel J. Rizzo,[†] Jingwei Jiang,[†] Dharati Joshi,[†] Gregory Veber,[†] Christopher Bronner, Rebecca A. Durr, Peter H. Jacobse, Ting Cao, Alin Kalayjian, Henry Rodriguez, Paul Butler, Ting Chen, Steven G. Louie,* Felix R. Fischer,* and Michael F. Crommie*

Cite This: *ACS Nano* 2021, 15, 20633−20642

Read Online

ACCESS | Metrics & More | Article Recommendations | Supporting Information

ABSTRACT: **Bottom-up graphene nanoribbons (GNRs) have recently been shown to host nontrivial topological phases. Here, we report the fabrication and characterization of deterministic GNR quantum dots whose orbital character is defined by zero-mode states arising from nontrivial topological interfaces. Topological control was achieved through the synthesis and on-surface assembly of three distinct molecular precursors designed to exhibit structurally derived topological electronic states. Using a combination of low-temperature scanning tunneling microscopy and spectroscopy, we have characterized two GNR topological quantum dot arrangements synthesized under ultrahigh vacuum conditions. Our results are supported by density-functional theory and tight-binding calculations, revealing that the magnitude and sign of orbital hopping between topological zero-mode states can be tuned based on the bonding geometry of the interconnecting region. These results demonstrate the utility of topological zero modes as components for designer quantum dots and advanced electronic devices.**

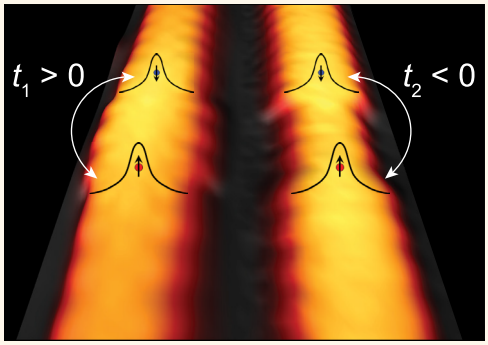

KEYWORDS: *graphene nanoribbons, topological materials, heterojunctions, quantum dots, scanning tunneling microscopy, scanning tunneling spectroscopy, density functional theory*

The advent of atomically precise bottom-up growth of graphene nanoribbons (GNRs)[1] has enabled realization of numerous well-defined GNR structures possessing a wide range of material and electronic properties originating from the rational design of molecular precursors. For example, this approach has been broadly applied to successfully synthesize tailored GNRs with a variety of widths,[2−4] edge structures,[5−7] and heteroatom dopants[8−14] at the atomic scale. Multiple synthetic strategies for achieving GNR heterostructures from monomeric precursors have been demonstrated, including the introduction of ancillary chemical reactions to GNRs derived from a single molecular precursor[15−19] and copolymerization of distinct but chemically compatible precursor monomers.[20−26] GNR heterostructures have also been exploited to create quantum dots[18,20,23,24] that possess electronic structures dependent on the size and shape of constituent GNR segments (i.e., where the behavior is determined by randomly connected segments of arbitrary length). Hierarchical growth[22] and sterically enforced selective copolymerization,[27] on the other hand, represent viable routes for creating deterministic GNR quantum dots, but have not yet been explored in this context.

The discovery of distinct topological phases[28] in GNRs and recent experimental[26,27] and theoretical[28−31] developments in engineering GNR topology have prompted a paradigm shift in the design and fabrication of GNR electronic structure. From this perspective, every periodic GNR structure possesses an invariant topological classification that is characteristic of its terminating unit cell and associated symmetries (e.g., a $\mathbb{Z}_2$ invariant for time reversal and spatial symmetries[28−30] and a $\mathbb{Z}$ invariant for chiral symmetry[31]). The bulk-boundary correspondence principle then dictates that an interface between two GNRs possessing different topological invariants will host a topological zero mode: a protected state that lies energetically at or near midgap and may be associated with a localized spin under suitable conditions.[28,31,32] The creation and controlled hybridization of neighboring zero modes[28] has been validated as a viable strategy for experimentally realizing small-gap semiconducting[26,27] and metallic[33] GNRs, as well as nanoporous graphene[34] wherein the frontier electronic

Received: October 26, 2021
Accepted: November 22, 2021
Published: November 29, 2021

structure is composed of topological zero-mode bands. By extension, isolated topological zero modes should provide a well-defined basis for realizing topological quantum dots (TQDs) embedded in extended GNR structures that are potentially suitable for applications such as tunneling field-effect transistors.[35]

Here, we report the deterministic growth and electronic structure characterization of GNR quantum dots composed of pairs of topological zero-mode states that appear at the interfaces between seven- and nine-atom-wide armchair GNRs (7-AGNRs and 9-AGNRs, respectively) as predicted theoretically in ref 28. We have made use of a bifunctional molecular linker previously used to generate 7/9-AGNR superlattices,[27] and we have discovered that it is synthetically compatible with specific 7- and 9-AGNR precursors. The 9-AGNR precursor used here was specifically designed for this study to permit viable copolymerization with the bifunctional linker into ordered nanostructures. The resulting GNRs exhibit pristine 7- and 9-AGNR segments connected by well-defined interfaces. These reproducible heterojunctions are separated by a fixed distance, thereby ensuring the creation of topological zero modes that hybridize across defined AGNR segments with predetermined electron hopping amplitudes. Since the low-energy spectra of quantum dots defined by coupled zero modes are ultimately determined by these hopping amplitudes, all TQDs synthesized through this reproducible methodology possess the same electronic structure—in contrast to the random GNR quantum dot structures realized previously through nondeterministic synthetic approaches.[18,20] We have performed experimental characterization of two varieties of GNR TQDs using scanning tunneling microscopy and spectroscopy (STM/STS) and reveal how TQD zero-mode splitting depends on the width of the intermediate GNR segment. These results are supported by first-principles density functional theory (DFT) and tight-binding (TB) calculations which provide additional insight into the physical origins of the magnitude and sign of the hopping terms that encode the energetic splitting and wave function character of the topological quantum dot states. These results provide the groundwork for achieving future magnetic spin centers with deterministic coupling using similar synthetic approaches.

RESULTS AND DISCUSSION

Our design for GNR quantum dots is based on a topologically nontrivial junction[28] that enables controlled bridging between 7-AGNR and 9-AGNR segments. To achieve this, we selected interfacial unit cells for the adjacent GNR segments that correspond to different topological classifications. The two unit cells are based on the zigzag′ (for 7-AGNRs) and zigzag (for 9-AGNRs) terminating unit cells,[28] which both possess mirror and inversion symmetry and can therefore be classified with a $\mathbb{Z}_2$ invariant (Figure 1A). In addition to the $\mathbb{Z}_2$ classification scheme, the approximate chiral symmetry of all periodic graphene-based materials also permits assignment of a $\mathbb{Z}$ invariant to these structures[31] (also shown in Figure 1A). While a non-zero difference in the value of $\mathbb{Z}_2$ across an interface in one-dimension (1D) indicates the presence of an odd number of topological interface states, the absolute value of the difference in $\mathbb{Z}$ provides the exact number of such interface states. As seen in Figure 1A, predictions based on both of these topological classification schemes are consistent with one zero-mode state being present at the interface of the

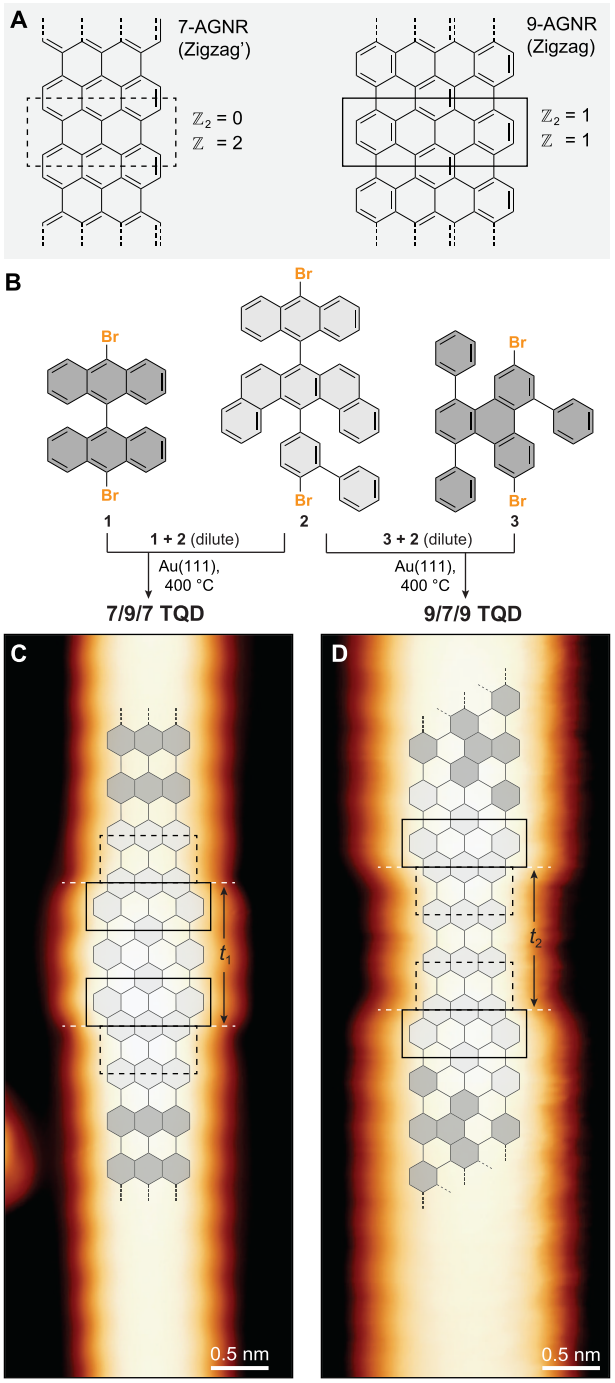

Figure 1. On-surface synthesis of AGNR topological quantum dots. (A) Topological invariants $\mathbb{Z}_2$ and $\mathbb{Z}$ for the depicted AGNRs are determined by the terminating unit cell and are associated with mirror/inversion symmetry and chiral symmetry, respectively. The zigzag termination of 7-AGNRs (dashed box, left panel) possesses topological invariants $\mathbb{Z}_2 = 0$ and $\mathbb{Z} = 2$, while the zigzag termination of 9-AGNRs (solid box, right panel) possesses topological invariants $\mathbb{Z}_2 = 1$ and $\mathbb{Z} = 1$. Crossing an interface as depicted by the structures in (C) and (D) between these two unit cells corresponds to a change in both topological invariants. Therefore, such an interface is expected to host a topological zero-mode state. (B) Molecular precursors 1 and 3 generate extended sections of 7-AGNRs and 9-AGNRs, respectively. Precursor 2 polymerizes to form a well-defined interface between the two structures in (A). Combining 1 (3) with dilute quantities of 2 yields extended segments of 7-AGNR (9-AGNR) with two

https://doi.org/10.1021/acsnano.1c09503
ACS Nano 2021, 15, 20633−20642

Figure 1. continued

topological interfaces separated by a rationally designed length of 9-AGNR (7-AGNR) and yields a 7/9/7 (9/7/9) topological quantum dot. (C) Structures of the 7/9/7 and (D) 9/7/9 topological quantum dots superimposed on the corresponding STM topographic images ((C): V_s = 0.60 V, I_t = 90 pA; (D): V_s = −0.30 V, I_t = 8 nA). T = 4 K for all measurements.

7-AGNR and 9-AGNR unit cells whose structure is shown in Figure 1.

In order to generate the specific 7/9-AGNR interface that is predicted to give rise to this zero-mode state[28,31] (Figures 1C,D), we employed a stepwise synthesis based on the codeposition of the bifunctional linker with the monomer for either 7- or 9-AGNRs on a Au(111) surface under ultrahigh vacuum (UHV) conditions (Figure 1B). In the first step, dilute quantities of the bifunctional linker **2** are deposited onto a clean Au(111) surface along with an excess of either precursor **1** or **3** (which constitute the 7- and 9-AGNR bulk, respectively). During radical step-growth polymerization of these mixtures, polymerization of bulk 7- or 9-AGNR precursors is the dominant process since they are present in much higher quantities than the bifunctional linker. Concurrently, dilute quantities of the bifunctional molecular linker **2** codeposited on the same surface dimerize. If we designate the side featuring the bromoanthracene group as the A side of the bifunctional linker and the bromobiphenyl group the B side, then the dimerization of **2** can lead to two possible structures featuring an AB−BA bond (dimers are linked by the biphenyl groups) or a BA−AB bond (dimers are linked by the bromoanthracene groups). The unreacted ends of these dimers can continue to bond with bulk 7- or 9-AGNR proto-polymer segments (Figure 1B), respectively. Further annealing results in fully graphenized pairs of GNR topological interfaces, where monomer **1** (**3**) bonds with the AB−BA (BA−AB) dimers to yield extended 7-AGNR (9-AGNR) segments interrupted by a segment of three 9-AGNR (7-AGNR) unit cells (Figure 1C,D). We refer to these structures as 7/9/7 and 9/7/9 TQDs, respectively. While the syntheses and on-surface polymerizations of precursors **1** and **2** have been reported previously,[1,27] molecular precursor **3** was designed specifically for this study. A low vapor pressure alternative to the 1,1′:2′,1′′-terphenyl-based 9-AGNR precursors,[2] **3** not only allows for easier sample preparation but more importantly is structurally compatible with the bifunctional linker **2**. Initial experiments had shown that molecular precursors for 9-AGNRs derived from 3′,6′-dibromo- or 3′,6′-diiodo-1,1′:2′,1′′-terphenyl (monomer **4** in Figure S1)[2] formed amorphous carbon networks in the presence of **1** or **2** rather than extended ribbons (Figure S1). Therefore, design and synthesis of **3** was necessary to realize interfaces between extended segments of 9-AGNR with junctions derived from **2**. A detailed description of the synthesis of precursor **3** can be found in Scheme S1.

STM topographic images of both 7/9/7 TQDs (Figure 1C) and 9/7/9 TQDs (Figure 1D) show characteristic width modulations along the GNR axis consistent with short segments of three-unit-cells of either 9-AGNR (in the case the 7/9/7 TQD) or 7-AGNR (in the case of the 9/7/9 TQD). Characteristic overview images of the as-deposited precursors and fully aromatized GNRs can be found in Figure S2. While the predominant species on the surface are homopolymeric 7- or 9-AGNRs, a small population feature the desired TQDs. We note that a codeposition of both 1 and 3 (the building blocks for 7- and 9-AGNRs) with the bifunctional linker 2 lead to unplanned, complex GNR mixtures upon annealing, likely resulting from surface-catalyzed radical rearrangements (Figure S3). However, single-junction structures are realized by replacing monomer **3** with molecular precursors that generate chevron-type GNRs (Figure S4).[1]

In order to probe the electronic properties of GNR TQDs, we performed STS point spectroscopy measurements and differential conductance (dI/dV) mapping on both types of GNR TQDs. These measurements directly probe the energy- and spatial-dependence of the local density of states (LDOS) of each GNR structure. Figure 2A shows that point spectra collected on the bulk 7-AGNR segment of 7/9/7 TQDs exhibit two prominent features at −0.8 and 1.6 V (features 1 and 4; red curve) that are consistent with previously reported STS measurements of the valence and conduction band edges of pure 7-AGNRs.[36] In contrast, point spectra collected in the 7/9/7 TQD junction region show two low-energy states at −0.1 and 0.6 V (features 2 and 3; blue curve) that appear within the bulk 7-AGNR energy gap. dI/dV maps collected at the energies associated with these features demonstrate that states at 1 and 4 are localized mainly on the bulk 7-AGNR segments while states at 2 and 3 are localized to the 7/9-AGNR junctions (Figure 2B). The LDOS for the lower energy state 2 shows a uniform high intensity throughout the short 9-AGNR segment (i.e., an antinode) linking the two topological interface states, while state 3 shows a diminished intensity in the same region (i.e., a node). The energetic alignment and spatial characteristics of states 2 and 3 suggests that they arise from hybridization between the two topological junction states. Simple quantum mechanical reasoning implies that the magnitude of the splitting between states 2 and 3 (E_{g1}) yields an experimental measure of the electron hopping amplitude (t_1) between the two topological junction states across the 9-AGNR segment: $|E_{g1}| = |2t_1| = 0.7$ eV.

We performed analogous STS measurements on a 9/7/9 TQD, which features the same 7/9 topological junctions as the 7/9/7 TQD, but with an inverted geometry (i.e., hybridization across a 7-AGNR segment). As before, four features can be observed in the point spectroscopy (features 5−8 in Figure 3A). States associated with features 5 and 8 are most prominent when the STM tip is placed above the bulk 9-AGNR segment (red curve), while states at 6 and 7 only appear in spectra collected in the region of the 7/9-AGNR junctions (blue curve). The energy gap between states 5 and 8 is consistent with previous STS measurements of pristine 9-AGNRs,[2] and dI/dV maps obtained at these energies show LDOS predominantly localized to the bulk 9-AGNR segments (Figure 3B). Conversely, dI/dV maps obtained at biases associated with in-gap states at 6 and 7 show localization on the 7/9-AGNR junction regions (Figure 3B), suggesting that states at 6 and 7 are associated with topological zero modes coupling through the short 7-AGNR segment. In this case, the lower energy state 6 features a node across the 7-AGNR segment while the higher energy state 7 shows the characteristics spatial LDOS associated with an antinode. This pattern of bonding and antibonding linear combinations is inverted when compared to the nodal patterns observed for the in-gap states 2 and 3 associated with the 7/9/7 TQD (Figure 2B). The energy gap between in-gap states 6 and 7 implies that the electron hopping amplitude between topological junction

https://doi.org/10.1021/acsnano.1c09503
ACS Nano 2021, 15, 20633−20642

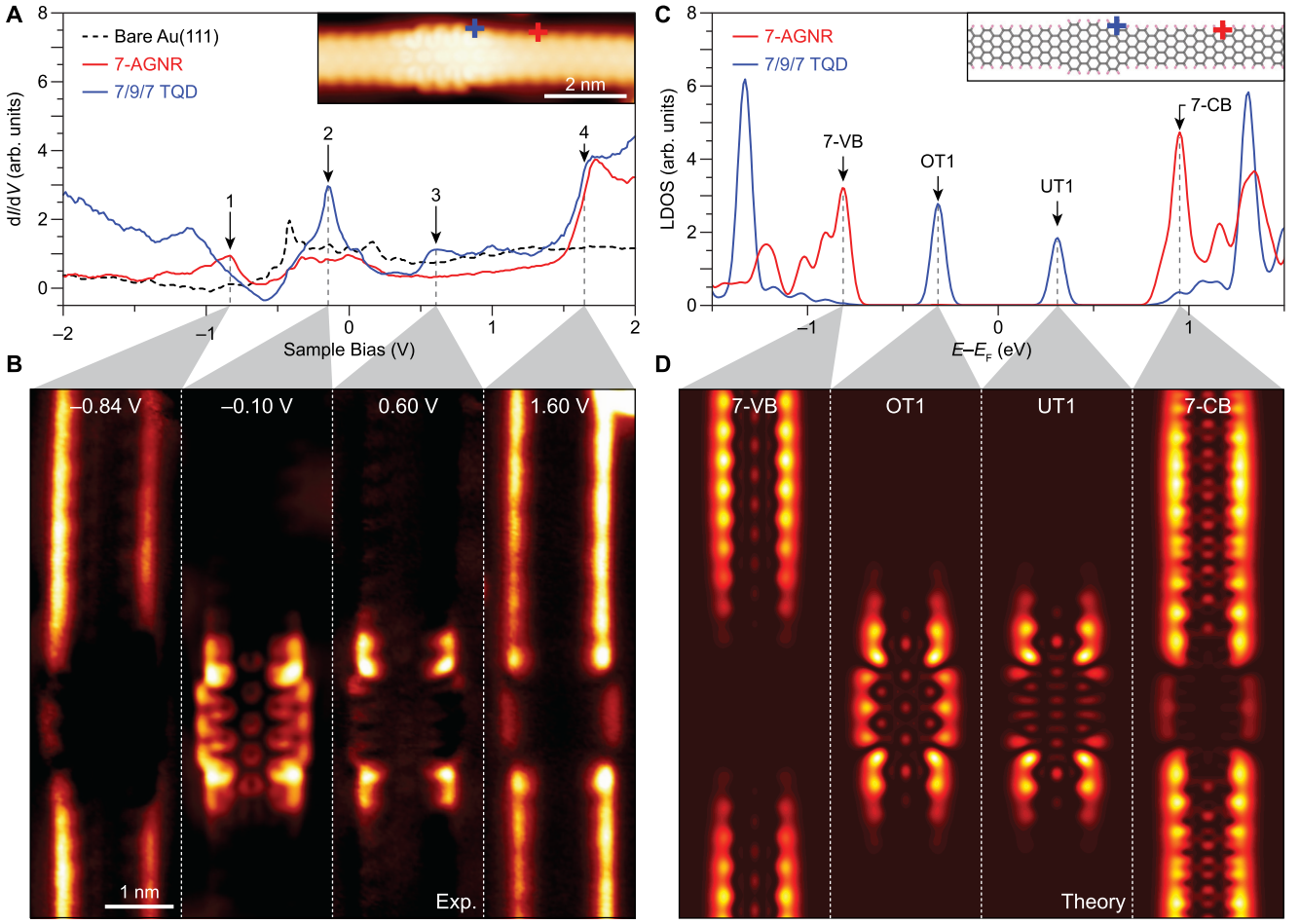

Figure 2. Electronic structure of 7/9/7 topological quantum dot. (A) Inset: STM topographic image of the 7/9/7 topological quantum dot (V_s = −0.10 V, I_t = 90 pA). dI/dV point spectroscopy conducted on the 7-AGNR bulk and the 7/9/7 TQD are plotted in red and blue, respectively, as indicated by the crosses in the inset. The dashed black curve corresponds to a reference spectrum conducted on bare Au(111). For all point spectra, V_{AC} = 10 mV. (B) dI/dV maps of the 7/9/7 TQD conducted at the indicated biases corresponding to peaks in (A) (I_t = 90 pA, V_{AC} = 20 mV). (C) DFT-LDA calculated LDOS for the theoretical 7/9/7 TQD structure shown in Figure S10A. The blue and red curves correspond to LDOS sampled over the regions indicated by the blue and red crosses in the inset, respectively (spectrum broadened by 10 meV Gaussian). (D) DFT-calculated LDOS maps of the 7/9/7 TQD at each of the four peak energies indicated in (C). LDOS is sampled 4 Å above the GNR plane. T = 4 K for all measurements.

states across the short 7-AGNR segment is roughly one-seventh of that across the 9-AGNR segment: $|E_{g2}| = |2t_2| = 0.1$ eV. The values of both t_1 and t_2 obtained for these two TQDs are consistent with the measured band gap of a 7/9-AGNR superlattice (which provides a measure of the difference in their magnitudes).[27]

To better understand the wave function characteristics and energetic alignment of TQD states, we compute the electronic states in our TQDs using first-principles DFT calculations. GNR point spectra collected on the 7/9/7 TQD were modeled by evaluating the DFT LDOS located in the 7-AGNR bulk as well as at the 7/9-AGNR junction (as indicated by the crosses in the inset in Figure 2C). The theoretical LDOS sampled in the 7-AGNR bulk resulted in a prominent occupied-state peak associated with the bulk valence band (labeled 7-VB) and an unoccupied-state peak associated with the conduction band (labeled 7-CB), in reasonable alignment with experimental features 1 and 4. The theoretical LDOS sampled in the 7/9-AGNR junction region is dominated by two low-energy states that gap symmetrically about E_F (labeled occupied topological state 1 (OT1) and unoccupied topological state 1 (UT1)) and is in good agreement with experimental states 2 and 3. Figure 2D shows the theoretical LDOS maps for the 7-VB, OT1, UT1, and 7-CB states. The theoretical LDOS maps exhibit most of the salient features seen in the experimental data in Figure 2B, including the extending of the 7-VB and 7-CB states throughout the 7-AGNR bulk region and confinement of the OT1 and UT1 states to the topological junctions. Notably, the nodal structure of the theoretical OT1 and UT1 LDOS mirrors that of experimental states 2 and 3. These theoretical results support the conclusion that the four experimental STS peaks observed in the 7/9/7 TQD correspond to bulk 7-AGNR band edge van Hove singularities along with two in-gap topological states.

Theoretical analysis of the 9/7/9 TQD yields similar good physical understanding of the experimental data. Specifically, the LDOS in the 9-AGNR bulk shows peaks associated with the pristine 9-AGNR valence and conduction bands (9-VB and 9-CB of Figure 3C; red curve), while the LDOS in the 7/9 junction region reveals a pair of in-gap states (occupied and unoccupied topological state 2 (OT2 and UT2) of Figure 3C; blue curve). The theoretical LDOS maps for these four states (Figure 3D) also show agreement with the experimental dI/dV maps for features 5−8 (Figure 3B). For example, OT2 has a

https://doi.org/10.1021/acsnano.1c09503
ACS Nano 2021, 15, 20633−20642

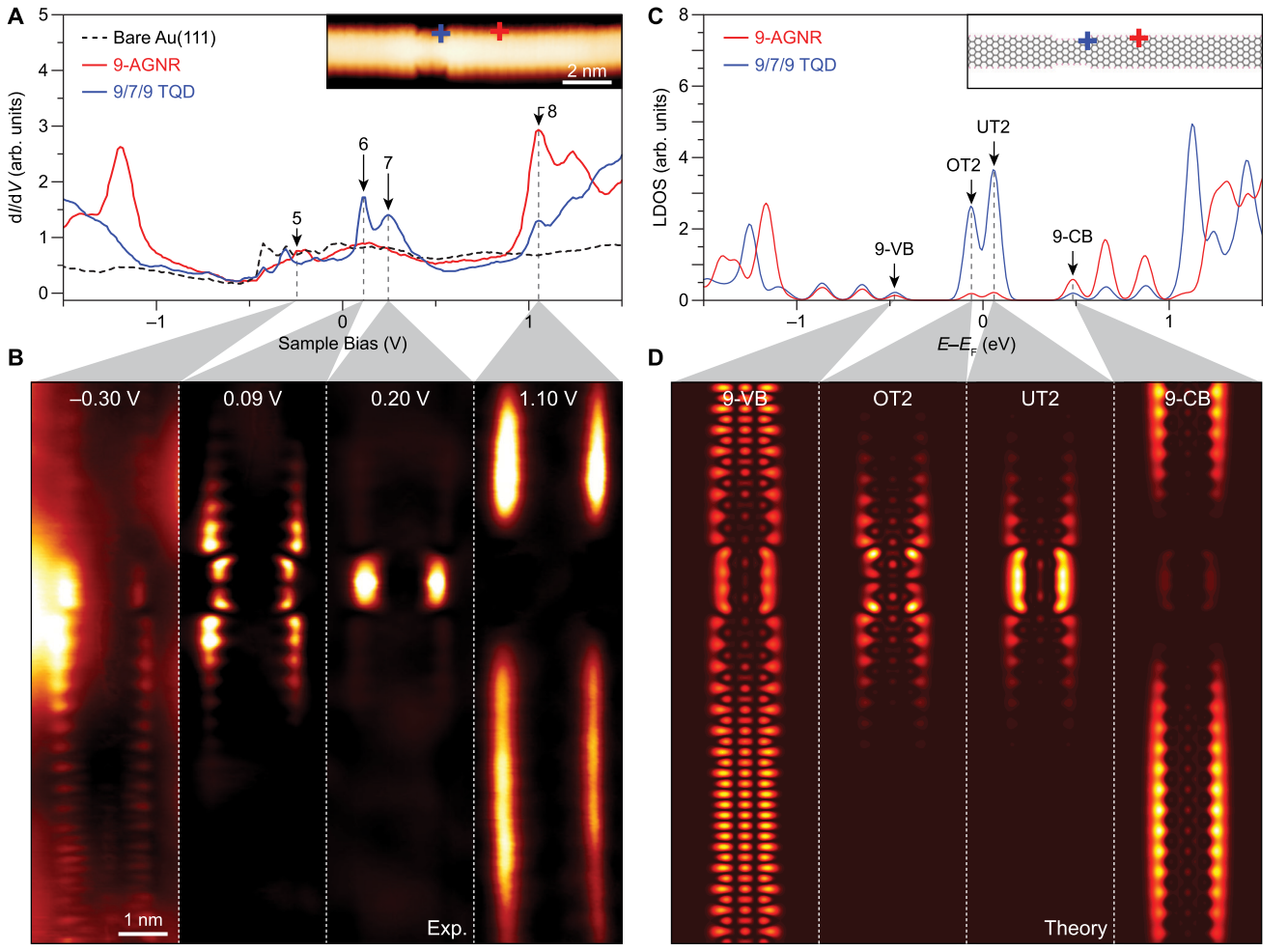

Figure 3. Electronic structure of 9/7/9 topological quantum dot. (A) Inset: STM topographic image of the 9/7/9 topological quantum dot (V_s = 0.20 V, I_t = 3 nA). dI/dV point spectroscopy conducted on the 9-AGNR bulk and the 9/7/9 TQD are plotted in red and blue, respectively, as indicated by the crosses in the inset. The dashed black curve corresponds to a reference spectrum conducted on bare Au(111). For all point spectra, V_{AC} = 10 mV. (B) dI/dV maps of the 9/7/9 TQD conducted at the indicated biases corresponding to peaks in (A) (state 5: I_t = 8 nA, V_{AC} = 20 mV; states 6−8: I_t = 3 nA, V_{AC} = 20 mV). (C) DFT-LDA calculated LDOS for the theoretical 9/7/9 TQD structure shown in Figure S10B. The blue and red curves correspond to LDOS sampled over the regions indicated by the blue and red crosses in the inset, respectively (spectrum broadened by 10 meV Gaussian). (D) DFT-calculated LDOS maps of the 9/7/9 TQD at each of the four peak energies indicated in (C). LDOS is sampled 4 Å above the GNR plane. T = 4 K for all measurements.

nodal line at the center of the 7-AGNR segment (similar to state 6 in Figure 3B), while UT2 shows an antinode (similar to state 7 in Figure 3B) (We note that states 6 and 7 both appear at positive bias rather than gapping symmetrically about V = 0 due to charge transfer with the underlying Au(111) surface as has been observed previously for AGNR-supported zero-mode states on Au(111)[26,27,37]). These theoretical results demonstrate that our experimental observations reflect the intrinsic topology-based electronic behavior of both 9/7/9 and 7/9/7 TQDs.

A useful analysis can be used to deconvolute the TQD states in the two quantum dots (QDs) in order to gain further insight into their energetic alignment and physical origin. We accomplish this by calculating the interface state for an isolated 7/9-AGNR topological junction (characterized by a zero mode at E_F) and using it as a basis state to build up the TQD in-gap state eigenfunctions. The top panel of Figure 4A shows the wave function for such an isolated zero mode with a 7/9 orientation (denoted $|\varphi_0^L\rangle$) which has a 7-AGNR segment on the left and a 9-AGNR segment on the right and is overlaid onto the left junction of a 7/9/7 TQD. The bottom panel of Figure 4A shows an isolated zero mode with the opposite 9/7 orientation overlaid onto the right 7/9/7 junction (denoted $|\varphi_0^R\rangle$). If these states interact via an electron hopping amplitude t_1, then the effective Hamiltonian is diagonalized by states of antisymmetric and symmetric linear combinations of $|\varphi_0^L\rangle$ and $|\varphi_0^R\rangle$ (Figure 4B) that possess eigenenergies $\pm t_1$ relative to E_F. These states are analogous to the UT1 and OT1 states shown in the 7/9/7 TQD *ab initio* energy level diagram (energies reproduced in Figure 4C). For a positive t_1, the symmetric state $\frac{1}{\sqrt{2}}[|\varphi_0^L\rangle + |\varphi_0^R\rangle]$ (which has zero nodes) is lower in energy than the antisymmetric state $\frac{1}{\sqrt{2}}[|\varphi_0^L\rangle - |\varphi_0^R\rangle]$ (which has one node) (Figure 4B). This is consistent with the experimental observation of Figure 2 that the TQD state with a central antinode (state 2) is lower in energy than the nodal state (state 3), and demonstrates that $t_1 > 0$.

When we repeat this process for the 9/7/9 TQD, we get a somewhat different result. Here, we label the left- and right-hand topological zero modes as $|\varphi'^L_0\rangle$ and $|\varphi'^R_0\rangle$ (Figure 4D), and once again introduce an electron hopping amplitude t_2

https://doi.org/10.1021/acsnano.1c09503
ACS Nano 2021, 15, 20633−20642

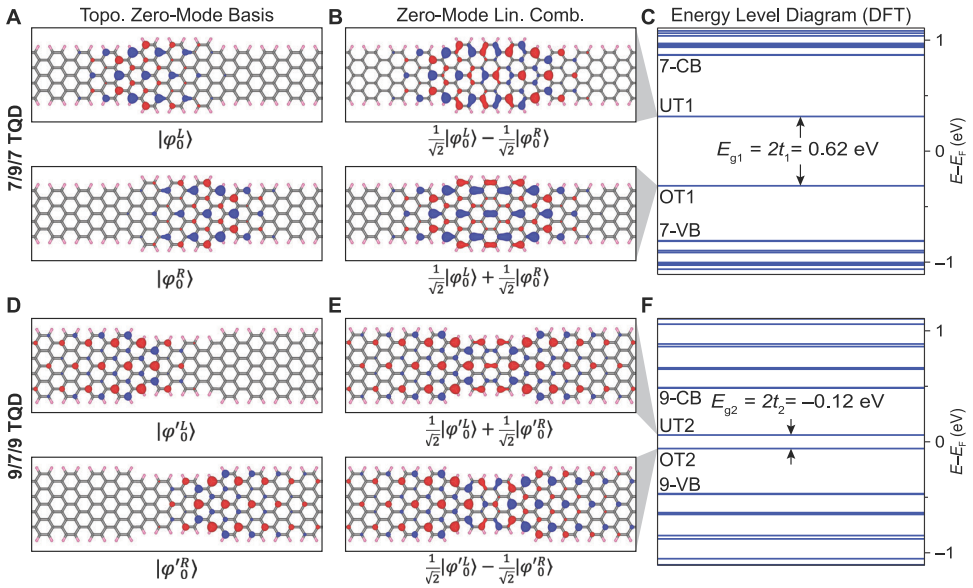

Figure 4. Emergence of quantum dot states from topological zero modes. (A) Left and right topological zero-mode basis states from isolated junctions ($|\varphi_0^L\rangle$ and $|\varphi_0^R\rangle$ in the top and bottom panels, respectively) superimposed on the 7/9/7 TQD chemical structure. Color indicates the sign of the phase factor. (B) Symmetric (bottom panel) and antisymmetric (top panel) linear combinations of zero-mode states shown in (A) correspond to the OT1 and UT1 states in the 7/9/7 TQD, respectively. (C) The DFT-LDA energy level diagram associated with a superlattice of a finite length theoretical 7/9/7 TQD structure (detailed structure in Figure S10A). The frontier energy levels originating from the 7-AGNR bulk are labeled 7-CB and 7-VB and the quantum dot states are UT1 and OT1. The energy splitting between UT1 and OT1 is equal to twice the electron hopping amplitude t_1 between $|\varphi_0^L\rangle$ and $|\varphi_0^R\rangle$. (D) Same as (A) but for the 9/7/9 TQD. Here the left and right zero-mode basis states are labeled $|\varphi'^L_0\rangle$ and $|\varphi'^R_0\rangle$ as shown in the top and bottom panels, respectively. (E) Same as (B) but for the 9/7/9 TQD. In contrast to the states shown in (B), the symmetric linear combination of zero-mode states has a higher energy than the antisymmetric linear combination. (F) Same as (C) but for the 9/7/9 TQD from a superlattice of the finite length structure shown in Figure S10B. Here the electron hopping amplitude t_2 between $|\varphi'^L_0\rangle$ and $|\varphi'^R_0\rangle$ is negative as dictated by the energy ordering of the symmetric and antisymmetric linear combinations of zero-mode states.

between them which causes splitting of the energy of the states around E_F and the formation of symmetric and antisymmetric linear combinations (Figure 4E). As expected, the symmetric state (top panel, Figure 4E) shows an antinode whereas the antisymmetric state has a central node. In contrast to the 7/9/7 case, however, the antisymmetric state $\frac{1}{\sqrt{2}}[|\varphi'^L_0\rangle - |\varphi'^R_0\rangle]$ (which corresponds to OT2) is a lower-energy eigenstate than the symmetric state $\frac{1}{\sqrt{2}}[|\varphi'^L_0\rangle + |\varphi'^R_0\rangle]$ (which corresponds to UT2) in both DFT and experiment. Hence, the electron hopping amplitude in this case is negative ($t_2 < 0$).

The fact that the hopping amplitudes of the 9/7/9 and 7/9/7 cases are opposite in sign is a consequence of the phase structure of the zero-mode wave function and the contrasting edge structures of the two TQDs (i.e., wide-narrow-wide versus narrow-wide-narrow, respectively). Following the procedure outlined in section 1 of the Supporting Information and Figure S5, one can write an explicit expression for the hopping amplitudes between the junction states in both TQDs in a p_z -orbital basis. By tracking the spatial variation of the phase on the p_z orbitals of the zero-mode wave functions along the junction edge, it can be seen that all non-zero terms in the analytical expression for t_1 are positive, whereas all non-zero terms for t_2 are negative. This is a general property of all topologically nontrivial junctions formed between coaxial n- and n+2-AGNRs with zigzag′/zigzag junctions where the middle segment is either an n+2 segment (resulting in $t_{eff} > 0$) or an n segment (resulting in $t_{eff} < 0$) under the constraint that n is odd (see the Supporting Information). Hence, the sign of the TQD junction-state hopping amplitude and likewise the symmetry of the associated topological quantum dot states can be tuned based on the width of the interconnecting region relative to the GNR bulk region.

The smaller energy splitting for the 9/7/9 TQD compared to the 7/9/7 TQD can be understood by inspecting the zero-mode wave function and noticing that its amplitude decays more rapidly in the central 7-AGNR regions compared to the decay of the wave function amplitude in the 9-AGNR regions (Figures 4A,D and S6). Therefore, the relative overlap between $|\varphi'^L_0\rangle$ and $|\varphi'^R_0\rangle$ across the 7-AGNR segment will be less than the overlap between $|\varphi_0^L\rangle$ and $|\varphi_0^R\rangle$ across the 9-AGNR segment, causing a reduction in the magnitude of t_2 compared to t_1. As expected, all four hybrid states in both TQDs possess a larger LDOS in the 9-AGNR regions compared to the 7-AGNR regions (Figure S6). This suggests that the necessary conditions for hosting magnetic states should be more readily achievable using the 9/7/9 scheme since the hopping amplitude is inherently smaller than in the 7/9/7 case. Since the hopping parameter should decay exponentially with the distance between topological interface states, one could realize a magnetic ground state by simply increasing separation between topological interface states. Indeed, first-principles calculations show that the 9/7/9 structure possesses an antiferromagnetic ground state with just five unit cells in the central segment, while the 7/9/7 structure requires 12 unit cells (Figure S7).

The ability to control the energy splitting and emergence of magnetic properties in GNR TQDs is thus ultimately dictated by the relative decay length of the constituent zero-mode wave functions on either side of topological heterojunctions.

https://doi.org/10.1021/acsnano.1c09503
ACS Nano 2021, 15, 20633−20642

Intuition based on conventional bulk wave function behavior suggests that the zero-mode decay length should be inversely proportional to the intrinsic GNR energy gap. Such phenomenology appears at first to be consistent with our experiment since topological junction states extend further into 9-AGNR regions compared to 7-AGNR regions (the latter having a band gap more than twice the former). However, closer scrutiny reveals that such intuition does not generally hold for all types of terminations and GNR junctions, where small changes in the atomic-scale interface structure can have a substantial impact on the spatial distribution of topological zero modes. For example, topological end states found at the zigzag termini of 7-AGNRs and 9-AGNRs have the opposite behavior, with the shorter decay length being found in the smaller band gap 9-AGNRs (Figure S8). In another example, if the registry of the zigzag′/zigzag 7/9-AGNR interface is shifted laterally, the resultant topological interface state will decay more rapidly on the 9-AGNR side of the interface compared to the 7-AGNR side (Figure S9). We have therefore developed a procedure for predicting zero-mode decay length for arbitrary GNR termini and heterojunctions based on the application of boundary conditions on sublattice polarized zero-mode states. Careful consideration of the wave function amplitude at each lattice site leads to a set of recursive equations whose solution yields the decay length (see sections 2 and 3 of the Supporting Information). This approach reveals that the decay length of topological zero-mode states is not determined by the bulk band gap of the host GNR, but rather by the interface geometry and the sublattice on which the topological zero-mode resides. Indeed, these structural factors can even conspire to completely localize topological interface states on the 7-AGNR side of a 7/9-AGNR heterojunction (Figure S9C,D).

CONCLUSIONS

We have developed an explicit protocol for generating rationally designed bottom-up GNR quantum dots based on topological boundary states, resulting in QD states of tunable hybridization and symmetry. The sterically selective on-surface copolymerization strategy used in this work allows for the development of GNR heterojunctions with customized interfacial geometries and tailored segment-lengths through use of a bifunctional linker previously used to generate GNR superlattices. We also demonstrate the ability to generate interfacial zero modes between GNRs derived from synthetically orthogonal molecular precursors using this specialized linker monomer. These results show that zero-dimensional topological states embedded in GNRs provide a platform for investigating designer topological behavior and quantum magnetism in molecular nanostructures and, thus, create opportunities for future nanoelectronics applications including sensors, transistors, and qubits.

EXPERIMENTAL METHODS

Molecular Synthesis. Syntheses of molecular precursors **1** and **2** were performed following previously reported protocols (refs 1 and 27, respectively). The synthesis of precursor **3** is detailed in the Supporting Information and Scheme S1.

On-Surface Preparation of GNR TQDs. Atomically clean Au(111) single crystals were prepared using several cycles of alternating Ar^+ sputtering and e-beam annealing to 500 °C. Surface cleanliness was confirmed by LT-STM measurements. All three molecular precursors were deposited onto a Au(111) surface under UHV conditions using home-built Knudsen cell evaporators sequentially starting with **2** and then either **1** or **3** in nominal ratios of at least 1:5 (areal fraction). Dilute quantities of **2** were first deposited using crucible temperatures of 210−235 °C for 30−90 min, resulting in enough molecular coverage to fully decorate step edges while leaving open terraces mostly bare. In order to grow the 7/9/7 (9/7/9) TQD, sufficient coverages of **1** (**3**) were achieved using a crucible temperature of 190 °C for 2 min (210 °C for 10 min). The relative molecular coverages were confirmed with STM topographic imaging prior to annealing. For both structures, the surface temperature was then gradually ramped (<2 K/min) using radiation heating to 200 °C and held there for 20 min to induce radical step-growth polymerization/copolymerization, and then subsequently ramped (<2 K/min) to 400 °C and held there for 20 min to fully planarize the GNR structures. For both preparations, since precursor **2** is present on the surface with either **1** or **3** prior to and throughout the growth process, radical copolymerization of **2** with the bulk precursors is permitted to take place during the first annealing step at 200 °C.

Scanning Tunneling Microscopy and Spectroscopy. All STM and STS experiments were conducted on a commercial CreaTec LT-STM system held at 4 K under UHV conditions. Chemically etched tungsten tips were used for all STM and STS experiments. STS measurements were recorded using a lock-in amplifier with modulation frequency f = 581 Hz and modulation amplitudes in the range V_{AC} = 10−20 mV. STS point spectra were conducted under open feedback loop conditions while dI/dV maps were conducted under constant current conditions. All STM tips were first calibrated using the Au(111) Shockley surface state[38] before STS measurements were performed. For each of the 7/9/7 and 9/7/9 TQDs, characteristic point spectra shown in Figures 2 and 3 were reproduced with at least 10 different tips on at least 3 distinct TQD structures using at least 100 individual spectra. All STM images were plotted using WSXM software.[39]

First-Principles DFT Calculations. First-principles DFT calculations were performed using the Quantum Espresso package.[40,41] We used norm conserving pseudopotentials with a 60 Ry energy cutoff. A 15 Å vacuum region was included in all three directions to prevent interactions between images of the finite structure containing the QD. All sp^2 dangling bonds at the edge of the carbon skeleton were hydrogenated. The structures were fully relaxed until all components of the force were smaller than 0.01 eV/ Å.

ASSOCIATED CONTENT

Supporting Information

The Supporting Information is available free of charge at https://pubs.acs.org/doi/10.1021/acsnano.1c09503.

Scheme for monomer **3** synthesis (along with ^{13}C and ^{1}H NMR of all intermediate compounds), STM images of step-by-step on-surface synthesis of TQDs and related experiments, derivation of analytical expressions for TQD hopping parameters, analytical procedures for calculating decay lengths of topological end and boundary states, model TQD unit cells used in DFT calculations, and description of the conditions for magnetism in TQD structures (PDF)

AUTHOR INFORMATION

Corresponding Authors

Steven G. Louie − *Department of Physics, University of California, Berkeley, California 94720, United States; Materials Sciences Division, Lawrence Berkeley National Laboratory, Berkeley, California 94720, United States;* orcid.org/0000-0003-0622-0170; Email: sglouie@berkeley.edu

https://doi.org/10.1021/acsnano.1c09503
ACS Nano 2021, 15, 20633−20642

Felix R. Fischer − *Materials Sciences Division, Lawrence Berkeley National Laboratory, Berkeley, California 94720, United States; Department of Chemistry, University of California, Berkeley, California 94720, United States; Kavli Energy NanoSciences Institute at the University of California Berkeley and the Lawrence Berkeley National Laboratory, Berkeley, California 94720, United States;* orcid.org/0000-0003-4723-3111; Email: ffischer@berkeley.edu

Michael F. Crommie − *Department of Physics, University of California, Berkeley, California 94720, United States; Materials Sciences Division, Lawrence Berkeley National Laboratory, Berkeley, California 94720, United States; Kavli Energy NanoSciences Institute at the University of California Berkeley and the Lawrence Berkeley National Laboratory, Berkeley, California 94720, United States;* orcid.org/0000-0001-8246-3444; Email: crommie@berkeley.edu

Authors

Daniel J. Rizzo − *Department of Physics, University of California, Berkeley, California 94720, United States; Department of Physics, Columbia University, New York, New York 10027, United States;* orcid.org/0000-0003-4587-4863

Jingwei Jiang − *Department of Physics, University of California, Berkeley, California 94720, United States; Materials Sciences Division, Lawrence Berkeley National Laboratory, Berkeley, California 94720, United States;* orcid.org/0000-0002-0949-4401

Dharati Joshi − *Department of Chemistry, University of California, Berkeley, California 94720, United States*

Gregory Veber − *Department of Chemistry, University of California, Berkeley, California 94720, United States*

Christopher Bronner − *Department of Physics, University of California, Berkeley, California 94720, United States*

Rebecca A. Durr − *Department of Chemistry, University of California, Berkeley, California 94720, United States*

Peter H. Jacobse − *Department of Physics, University of California, Berkeley, California 94720, United States*

Ting Cao − *Department of Physics, University of California, Berkeley, California 94720, United States; Department of Materials Science and Engineering, University of Washington, Seattle, Washington 98195, United States;* orcid.org/0000-0003-1300-6084

Alin Kalayjian − *Department of Chemistry, University of California, Berkeley, California 94720, United States*

Henry Rodriguez − *Department of Physics, University of California, Berkeley, California 94720, United States*

Paul Butler − *Department of Physics, University of California, Berkeley, California 94720, United States*

Ting Chen − *Department of Physics, University of California, Berkeley, California 94720, United States;* orcid.org/0000-0002-6616-0512

Complete contact information is available at: https://pubs.acs.org/10.1021/acsnano.1c09503

Author Contributions

†D.J.R., J.J., D.J., and G.V. contributed equally to this work. D.J.R, P.H.J., C.B., H.R., P.B., and T. Chen performed on-surface syntheses and STM/STS experiments. D.J.R. performed the analysis of STM/STS data. M.F.C. oversaw and advised scanning probe and on-surface synthesis experiments. R.A.D. performed the synthesis of molecular precursor **1**. G.V. developed and performed the synthesis of bifunctional linker **2**. R.A.D., A.M.K., and D.J. developed and performed the synthesis of molecular precursor **3**. F.R.F. oversaw and advised synthetic protocols. J.J. and T. Cao performed first-principles DFT calculations and tight-binding analyses. S.G.L. oversaw and advised topological analyses and *ab initio* calculations.

Notes

The authors declare no competing financial interest.

All data presented in the manuscript are available upon request.

ACKNOWLEDGMENTS

This work was funded by the US Department of Energy, Office of Science, Office of Basic Energy Sciences, Materials Sciences and Engineering Division under contract no. DE-AC02-05-CH11231 (Nanomachine program: KC1203) (molecular self-assembly, STM imaging, DFT calculations). Support also provided by the Office of Naval Research under MURI Program N00014-19-1-2596 (STM spectroscopy), by the Office of Naval Research under N00014-19-1-2503 (synthesis of bifunctional linker **2**), and the National Science Foundation under grants DMR-1839098 (effective Hamiltonian model, synthesis of molecular precursors **1**, and **3**) and DMR-1926004 (tight-binding analysis). The Computational resources were provided by the Department of Energy at Lawrence Berkeley National Laboratory's NERSC facility, the National Science Foundation through XSEDE resources at NICS, and through Frontera computing project at the Texas Advanced Computing Center under Award No. OAC-1818253. P.H.J. acknowledges fellowship support from the Dutch Research Council (NWO) through Rubicon Award no. 019.182EN.18.

REFERENCES

(1) Cai, J.; Ruffieux, P.; Jaafar, R.; Bieri, M.; Braun, T.; Blankenburg, S.; Muoth, M.; Seitsonen, A. P.; Saleh, M.; Feng, X.; Müllen, K.; Fasel, R. Atomically Precise Bottom-Up Fabrication of Graphene Nanoribbons. *Nature* **2010**, *466*, 470.

(2) Talirz, L.; Söde, H.; Dumslaff, T.; Wang, S.; Sanchez-Valencia, J. R.; Liu, J.; Shinde, P.; Pignedoli, C. A.; Liang, L.; Meunier, V.; Plumb, N. C.; Shi, M.; Feng, X.; Narita, A.; Müllen, K.; Fasel, R.; Ruffieux, P. On-Surface Synthesis and Characterization of 9-Atom Wide Armchair Graphene Nanoribbons. *ACS Nano* **2017**, *11*, 1380−1388.

(3) Kimouche, A.; Ervasti, M. M.; Drost, R.; Halonen, S.; Harju, A.; Joensuu, P. M.; Sainio, J.; Liljeroth, P. Ultra-Narrow Metallic Armchair Graphene Nanoribbons. *Nat. Commun.* **2015**, *6*, 10177.

(4) Chen, Y.-C.; de Oteyza, D. G.; Pedramrazi, Z.; Chen, C.; Fischer, F. R.; Crommie, M. F. Tuning the Band Gap of Graphene Nanoribbons Synthesized from Molecular Precursors. *ACS Nano* **2013**, *7*, 6123−6128.

(5) Ruffieux, P.; Wang, S.; Yang, B.; Sánchez-Sánchez, C.; Liu, J.; Dienel, T.; Talirz, L.; Shinde, P.; Pignedoli, C. A.; Passerone, D.; Dumslaff, T.; Feng, X.; Müllen, K.; Fasel, R. On-Surface Synthesis of Graphene Nanoribbons with Zigzag Edge Topology. *Nature* **2016**, *531*, 489.

(6) Liu, J.; Li, B.-W.; Tan, Y.-Z.; Giannakopoulos, A.; Sanchez-Sanchez, C.; Beljonne, D.; Ruffieux, P.; Fasel, R.; Feng, X.; Müllen, K. Toward Cove-Edged Low Band Gap Graphene Nanoribbons. *J. Am. Chem. Soc.* **2015**, *137*, 6097−6103.

(7) de Oteyza, D. G.; García-Lekue, A.; Vilas-Varela, M.; Merino-Díez, N.; Carbonell-Sanromà, E.; Corso, M.; Vasseur, G.; Rogero, C.; Guitián, E.; Pascual, J. I.; Ortega, J. E.; Wakayama, Y.; Peña, D. Substrate-Independent Growth of Atomically Precise Chiral Graphene Nanoribbons. *ACS Nano* **2016**, *10*, 9000−9008.

(8) Cloke, R. R.; Marangoni, T.; Nguyen, G. D.; Joshi, T.; Rizzo, D. J.; Bronner, C.; Cao, T.; Louie, S. G.; Crommie, M. F.; Fischer, F. R. Site-Specific Substitutional Boron Doping of Semiconducting Arm-

chair Graphene Nanoribbons. *J. Am. Chem. Soc.* **2015**, *137*, 8872−8875.
(9) Kawai, S.; Saito, S.; Osumi, S.; Yamaguchi, S.; Foster, A. S.; Spijker, P.; Meyer, E. Atomically Controlled Substitutional Boron-Doping of Graphene Nanoribbons. *Nat. Commun.* **2015**, *6*, 8098.
(10) Nguyen, G. D.; Toma, F. M.; Cao, T.; Pedramrazi, Z.; Chen, C.; Rizzo, D. J.; Joshi, T.; Bronner, C.; Chen, Y.-C.; Favaro, M.; Louie, S. G.; Fischer, F. R.; Crommie, M. F. Bottom-Up Synthesis of N = 13 Sulfur-Doped Graphene Nanoribbons. *J. Phys. Chem. C* **2016**, *120*, 2684−2687.
(11) Wang, X.-Y.; Urgel, J. I.; Barin, G. B.; Eimre, K.; Di Giovannantonio, M.; Milani, A.; Tommasini, M.; Pignedoli, C. A.; Ruffieux, P.; Feng, X.; Fasel, R.; Müllen, K.; Narita, A. Bottom-Up Synthesis of Heteroatom-Doped Chiral Graphene Nanoribbons. *J. Am. Chem. Soc.* **2018**, *140*, 9104−9107.
(12) Vo, T. H.; Perera, U. G. E.; Shekhirev, M.; Mehdi Pour, M.; Kunkel, D. A.; Lu, H.; Gruverman, A.; Sutter, E.; Cotlet, M.; Nykypanchuk, D.; Zahl, P.; Enders, A.; Sinitskii, A.; Sutter, P. Nitrogen-Doping Induced Self-Assembly of Graphene Nanoribbon-Based Two-Dimensional and Three-Dimensional Metamaterials. *Nano Lett.* **2015**, *15*, 5770−5777.
(13) Bronner, C.; Stremlau, S.; Gille, M.; Brauße, F.; Haase, A.; Hecht, S.; Tegeder, P. Aligning the Band Gap of Graphene Nanoribbons by Monomer Doping. *Angew. Chem., Int. Ed.* **2013**, *52*, 4422−4425.
(14) Durr, R. A.; Haberer, D.; Lee, Y.-L.; Blackwell, R.; Kalayjian, A. M.; Marangoni, T.; Ihm, J.; Louie, S. G.; Fischer, F. R. Orbitally Matched Edge-Doping in Graphene Nanoribbons. *J. Am. Chem. Soc.* **2018**, *140*, 807−813.
(15) Rizzo, D. J.; Wu, M.; Tsai, H.-Z.; Marangoni, T.; Durr, R. A.; Omrani, A. A.; Liou, F.; Bronner, C.; Joshi, T.; Nguyen, G. D.; Rodgers, G. F.; Choi, W.-W.; Jørgensen, J. H.; Fischer, F. R.; Louie, S. G.; Crommie, M. F. Length-Dependent Evolution of Type II Heterojunctions in Bottom-Up-Synthesized Graphene Nanoribbons. *Nano Lett.* **2019**, *19*, 3221−3228.
(16) Nguyen, G. D.; Tsai, H.-Z.; Omrani, A. A.; Marangoni, T.; Wu, M.; Rizzo, D. J.; Rodgers, G. F.; Cloke, R. R.; Durr, R. A.; Sakai, Y.; Liou, F.; Aikawa, A. S.; Chelikowsky, J. R.; Louie, S. G.; Fischer, F. R.; Crommie, M. F. Atomically Precise Graphene Nanoribbon Heterojunctions from a Single Molecular Precursor. *Nat. Nanotechnol.* **2017**, *12*, 1077.
(17) Ma, C.; Liang, L.; Xiao, Z.; Puretzky, A. A.; Hong, K.; Lu, W.; Meunier, V.; Bernholc, J.; Li, A.-P. Seamless Staircase Electrical Contact to Semiconducting Graphene Nanoribbons. *Nano Lett.* **2017**, *17*, 6241−6247.
(18) Wang, S.; Kharche, N.; Costa Girão, E.; Feng, X.; Müllen, K.; Meunier, V.; Fasel, R.; Ruffieux, P. Quantum Dots in Graphene Nanoribbons. *Nano Lett.* **2017**, *17*, 4277−4283.
(19) Marangoni, T.; Haberer, D.; Rizzo, D. J.; Cloke, R. R.; Fischer, F. R. Heterostructures through Divergent Edge Reconstruction in Nitrogen-Doped Segmented Graphene Nanoribbons. *Chem. - Eur. J.* **2016**, *22*, 13037−13040.
(20) Chen, Y.-C.; Cao, T.; Chen, C.; Pedramrazi, Z.; Haberer, D.; de Oteyza, D. G.; Fischer, F. R.; Louie, S. G.; Crommie, M. F. Molecular Bandgap Engineering of Bottom-Up Synthesized Graphene Nanoribbon Heterojunctions. *Nat. Nanotechnol.* **2015**, *10*, 156.
(21) Cai, J.; Pignedoli, C. A.; Talirz, L.; Ruffieux, P.; Söde, H.; Liang, L.; Meunier, V.; Berger, R.; Li, R.; Feng, X.; Müllen, K.; Fasel, R. Graphene Nanoribbon Heterojunctions. *Nat. Nanotechnol.* **2014**, *9*, 896.
(22) Bronner, C.; Durr, R. A.; Rizzo, D. J.; Lee, Y.-L.; Marangoni, T.; Kalayjian, A. M.; Rodriguez, H.; Zhao, W.; Louie, S. G.; Fischer, F. R.; Crommie, M. F. Hierarchical On-Surface Synthesis of Graphene Nanoribbon Heterojunctions. *ACS Nano* **2018**, *12*, 2193−2200.
(23) Pedramrazi, Z.; Chen, C.; Zhao, F.; Cao, T.; Nguyen, G. D.; Omrani, A. A.; Tsai, H.-Z.; Cloke, R. R.; Marangoni, T.; Rizzo, D. J.; Joshi, T.; Bronner, C.; Choi, W.-W.; Fischer, F. R.; Louie, S. G.; Crommie, M. F. Concentration Dependence of Dopant Electronic Structure in Bottom-Up Graphene Nanoribbons. *Nano Lett.* **2018**, *18*, 3550−3556.
(24) Carbonell-Sanromà, E.; Brandimarte, P.; Balog, R.; Corso, M.; Kawai, S.; Garcia-Lekue, A.; Saito, S.; Yamaguchi, S.; Meyer, E.; Sánchez-Portal, D.; Pascual, J. I. Quantum Dots Embedded in Graphene Nanoribbons by Chemical Substitution. *Nano Lett.* **2017**, *17*, 50−56.
(25) Sun, Q.; Yao, X.; Gröning, O.; Eimre, K.; Pignedoli, C. A.; Müllen, K.; Narita, A.; Fasel, R.; Ruffieux, P. Coupled Spin States in Armchair Graphene Nanoribbons with Asymmetric Zigzag Edge Extensions. *Nano Lett.* **2020**, *20*, 6429−6436.
(26) Gröning, O.; Wang, S.; Yao, X.; Pignedoli, C. A.; Borin Barin, G.; Daniels, C.; Cupo, A.; Meunier, V.; Feng, X.; Narita, A.; Müllen, K.; Ruffieux, P.; Fasel, R. Engineering of Robust Topological Quantum Phases in Graphene Nanoribbons. *Nature* **2018**, *560*, 209−213.
(27) Rizzo, D. J.; Veber, G.; Cao, T.; Bronner, C.; Chen, T.; Zhao, F.; Rodriguez, H.; Louie, S. G.; Crommie, M. F.; Fischer, F. R. Topological Band Engineering of Graphene Nanoribbons. *Nature* **2018**, *560*, 204−208.
(28) Cao, T.; Zhao, F.; Louie, S. G. Topological Phases in Graphene Nanoribbons: Junction States, Spin Centers, and Quantum Spin Chains. *Phys. Rev. Lett.* **2017**, *119*, 076401.
(29) Lee, Y.-L.; Zhao, F.; Cao, T.; Ihm, J.; Louie, S. G. Topological Phases in Cove-Edged and Chevron Graphene Nanoribbons: Geometric Structures, Z_2 Invariants, and Junction States. *Nano Lett.* **2018**, *18*, 7247−7253.
(30) Lin, K.-S.; Chou, M.-Y. Topological Properties of Gapped Graphene Nanoribbons with Spatial Symmetries. *Nano Lett.* **2018**, *18*, 7254−7260.
(31) Jiang, J.; Louie, S. G. Topology Classification Using Chiral Symmetry and Spin Correlations in Graphene Nanoribbons. *Nano Lett.* **2021**, *21*, 197.
(32) Wang, S.; Talirz, L.; Pignedoli, C. A.; Feng, X.; Müllen, K.; Fasel, R.; Ruffieux, P. Giant Edge State Splitting at Atomically Precise Graphene Zigzag Edges. *Nat. Commun.* **2016**, *7*, 11507.
(33) Rizzo, D. J.; Veber, G.; Jiang, J.; McCurdy, R.; Cao, T.; Bronner, C.; Chen, T.; Louie, S. G.; Fischer, F. R.; Crommie, M. F. Inducing Metallicity in Graphene Nanoribbons *via* Zero-Mode Superlattices. *Science* **2020**, *369*, 1597−1603.
(34) Jacobse, P. H.; McCurdy, R. D.; Jiang, J.; Rizzo, D. J.; Veber, G.; Butler, P.; Zuzak, R.; Louie, S. G.; Fischer, F. R.; Crommie, M. F. Bottom-Up Assembly of Nanoporous Graphene with Emergent Electronic States. *J. Am. Chem. Soc.* **2020**, *142*, 13507−13514.
(35) Vadlamani, S. K.; Agarwal, S.; Limmer, D. T.; Louie, S. G.; Fischer, F. R.; Yablonovitch, E. Tunnel-Fet Switching Is Governed by Non-Lorentzian Spectral Line Shape. *Proc. IEEE* **2020**, *108*, 1235−1244.
(36) Ruffieux, P.; Cai, J.; Plumb, N. C.; Patthey, L.; Prezzi, D.; Ferretti, A.; Molinari, E.; Feng, X.; Müllen, K.; Pignedoli, C. A.; Fasel, R. Electronic Structure of Atomically Precise Graphene Nanoribbons. *ACS Nano* **2012**, *6*, 6930−6935.
(37) Koch, M.; Ample, F.; Joachim, C.; Grill, L. Voltage-Dependent Conductance of a Single Graphene Nanoribbon. *Nat. Nanotechnol.* **2012**, *7*, 713−717.
(38) Chen, W.; Madhavan, V.; Jamneala, T.; Crommie, M. F. Scanning Tunneling Microscopy Observation of an Electronic Superlattice at the Surface of Clean Gold. *Phys. Rev. Lett.* **1998**, *80*, 1469−1472.
(39) Horcas, I.; Fernández, R.; Gómez-Rodríguez, J. M.; Colchero, J.; Gómez-Herrero, J.; Baro, A. M. Wsxm: A Software for Scanning Probe Microscopy and a Tool for Nanotechnology. *Rev. Sci. Instrum.* **2007**, *78*, 013705.
(40) Giannozzi, P.; Andreussi, O.; Brumme, T.; Bunau, O.; Buongiorno Nardelli, M.; Calandra, M.; Car, R.; Cavazzoni, C.; Ceresoli, D.; Cococcioni, M.; Colonna, N.; Carnimeo, I.; Dal Corso, A.; de Gironcoli, S.; Delugas, P.; DiStasio, R. A.; Ferretti, A.; Floris, A.; Fratesi, G.; Fugallo, G.; et al. Advanced Capabilities for Materials

https://doi.org/10.1021/acsnano.1c09503
ACS Nano 2021, 15, 20633−20642

Modelling with Quantum Espresso. *J. Phys.: Condens. Matter* **2017**, *29*, 465901.
(41) Giannozzi, P.; Baroni, S.; Bonini, N.; Calandra, M.; Car, R.; Cavazzoni, C.; Ceresoli, D.; Chiarotti, G. L.; Cococcioni, M.; Dabo, I.; Dal Corso, A.; de Gironcoli, S.; Fabris, S.; Fratesi, G.; Gebauer, R.; Gerstmann, U.; Gougoussis, C.; Kokalj, A.; Lazzeri, M.; Martin-Samos, L.; et al. Quantum Espresso: A Modular and Open-Source Software Project for Quantum Simulations of Materials. *J. Phys.: Condens. Matter* **2009**, *21*, 395502.

https://doi.org/10.1021/acsnano.1c09503
ACS Nano 2021, 15, 20633−20642